

Reply to the review of manuscript ACP-2012-707.

Monitoring volcanic ash cloud top height through simultaneous retrieval of optical data from polar orbiting and geostationary satellites

Klemen Zakšek, 16 January 2013

We would like to thank to the reviewer for carefully reading the paper and for the constructive comments. The answers on all remarks are below. The corrected manuscript (text only) is added in the end of this reply.

In this work the authors present a method to estimate volcanic ash cloud top heights (ACTH) using data from two satellite-based instruments, the geostationary SEVIRI and polar orbiting MODIS instruments. An image matching technique is described and applied to the Eyjafjallajökull eruption in April 2010. Besides of using two separate satellite instruments, the authors suggest two novel ideas: (1) ACTH is based on 'intersection line distance', allowing quality estimation, and (2) the effect of wind is minimized by using interpolation from two consecutive images from SEVIRI. The review of existing height estimate methods is extensive and clearly points out the strengths and limitations of different methods. However, the article lacks a quantitative comparison between the suggested new method and most of the existing ones. The article is moderately well written, and presents an interesting new application of the known stereo height estimate methods. I recommend the article to be published in ACP with slight modifications.

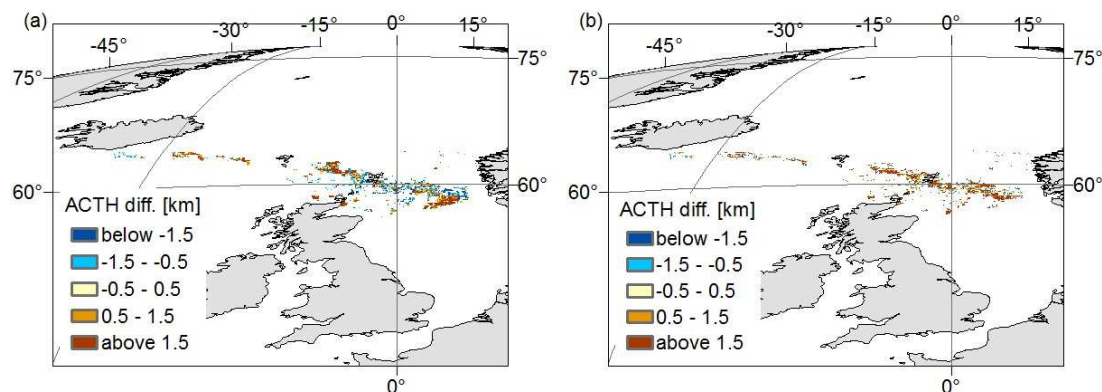
We estimate the accuracy of the proposed method analytically. Thus we included in the first manuscript only a comparison with ground data (radar) and MISR heights. Here we corrected the discussion and added additional comparison between our ACTH and standard MODIS cloud top height product (CO₂ slicing technique) and ACTH based on BT and temperature profile:

We compare our results also with the standard MODIS cloud product MOD06_L2 based on the CO₂ absorption technique (Platnick et al., 2003). Its spatial resolution is about 5 km. The product estimates the top of the cloud height pressure and not geometrical height. To convert the pressure into the geometrical height we use atmospheric sounding data for the location of Tórshavn (Faroe Islands; 62.01° N, 6.76° W) on 15 April 2010 at 12:00 UTC. The time of the atmospheric sounding is not the same as the time of MODIS retrieval (11:35 UTC; see fig. 8a). The valid plume pixels seem in general to be higher in our results than in the MOD06_L2 product (fig. 12 a). The bias equals approximately 650 m.

The same sounding data are used also to estimate ACTH with the BT method (fig. 12 b). Because the measured temperature in the sounding data fluctuates, it is possible to apply this sounding only for the clouds that are between 4 km and 11 km. The ash plume was in this range but the clouds around it not, thus fig. 12 compares ACTH only the area of the ash plume. The results of the BT method have a bias of 2200 m compared to the proposed method. A bias larger than 1000 m was observed already in similar previous studies (Genkova et al., 2007). The reason for the biases is in the retrieval of a

radiative height that does not estimate exactly the top of the cloud but the height of the “cloud centre”.

Figure 12. Comparison of the valid ACTH of the ash plume and the standard MODIS top height product (a) and results of the BT method (b) on Apr. 15th at 11:35 UTC (ACTH in fig. 8a).



Specific comments

1) Section 2.3: It is not explained how the ACTH is obtained by the absorption techniques. Can the method be briefly described?

We have corrected the method description into:

The CO₂ absorption (often named as slicing) technique is based on the atmosphere becoming more opaque due to CO₂ absorption as the wavelength increases. This causes radiances obtained from spectral bands between 11 and 15 μm to be sensitive to a different layer of the atmosphere.

2) Section 2.4: It is not mentioned what instruments have been used for obtaining ACTH using trajectories. What is required of these instruments (i.e. in terms of revisit times)? How do the result compare to those obtained by other methods?

We have added the following text to the method description:

The method usually applies low spatial resolution satellite instruments with revisit time of about 12 hours as for instance Infrared Atmospheric Sounding Interferometer – IASI (Klüser et al., 2013). In general any kind of instruments can be used as long as they provide the data required by the model. It is the model that "moves" the detected ash cloud back to its source, thus the quality of the model and meteorological data (wind velocity and direction as a function of height) are of highest importance.

Klüser, L., Erbertseder, T. and Meyer-Arne, J.: Observation of volcanic ash from Puyehue–Cordón Caulle with IASI, Atmospheric Measurement Techniques, 6(1), 35–46, doi:10.5194/amt-6-35-2013, 2013.

3) Section 3: It is not explicitly mentioned which channels of SEVIRI and MODIS are used in the image matching. Does the result depend on the choice of channels? Does the different path length in atmosphere have an effect?

Well, the used bands are mentioned in:

- abstract,
- second paragraph of Section 3,
- under Fig. 2

We always used only HRV band of SEVIRI and band 1 of MODIS. The results obviously depend on the selected bands because reflectivity is band. To make it clearer we have added a paragraph in discussion(5.1):

In general the results of image matching between datasets acquired by two different instruments depend also on the used spectral bands. If the ash and meteorological clouds do not have similar reflectivity in MODIS and SEVIRI spectral bands, image matching is likely to fail. Here we use SEVIRI HRV band that covers a large part of visible and near infrared spectrum. Furthermore, we used MODIS band 1 that covers only “red” spectrum of the visible light. The comparison of both datasets has shown that the data covering clouds and volcanic ash are highly correlated, which justifies bands’ selection. In addition, different atmospheric path length of SEVIRI and MODIS measurements does not influence the results.

4) Section 3.2: The description of the area-based image matching method (p. 25628-25629) is not very clear and needs clarification. Perhaps a schematic illustration of the method could be presented.

A large part of the section about areal image matching was rewritten. Here we provide some longer answer as well. Note that we changed the order of images (in original manuscript we were defined search subset in image 1 and reference subset in image 2 and now it is vice versa) – this makes no difference in computation but it might be easier for a reader to follow. Corrected text:

The method contains the following steps:

- Based on the pixel being currently processed (with image coordinates C, L) select a reference subset (with a number of columns n_{c1} and a number of lines n_{l1}) of the first image. This is shown in fig. 3 (left): pixel C, L is in red, the reference frame is yellow.
- In the second image select a search subset (with a number of columns $n_{c2} > n_{c1}$ and a number of lines $n_{l2} > n_{l1}$) that is centred over the pixel having the same image coordinates (C, L). This step merely reduces the possible extent of data subset from both images to be compared. Thus, it is theoretically not necessary but it reduces the computing time. The size of this search subset should be large enough to detect the largest expected shifts. Fig. 3 (right)

shows the search subset (light orange) in the second image centred at the pixel C, L . (dark orange).

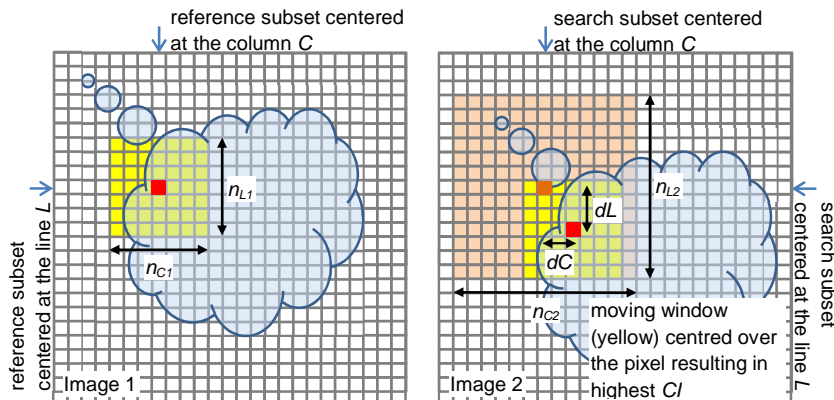
- Within the search subset define a moving window (with a number of columns n_{c2} and a number of lines n_{l2} – as large as the reference subset in the first image). The moving window is in fig. 3 (right) in yellow.
- Move this window across the search subset and for each possible shift of the moving window compute the normalized cross-covariance correlation CI between the reference subset of the first image and the moving window from the second image (Eq. 1):

$$CI = \frac{\sum_{i=n_{c1}/2-1, j=n_{l1}/2-1}^{i=n_{c1}/2-1, j=n_{l1}/2-1} (DNr_{i,j} - \mu r) \cdot (DNm_{i,j} - \mu s)}{\sqrt{\sum_{i=1-n_{c1}/2, j=1-n_{l1}/2}^{i=n_{c1}/2-1, j=n_{l1}/2-1} (DNr_{i,j} - \mu r)^2} \cdot \sqrt{\sum_{i=1-n_{c1}/2, j=1-n_{l1}/2}^{i=n_{c1}/2-1, j=n_{l1}/2-1} (DNm_{i,j} - \mu s)^2}}, \quad (1)$$

where CI is the correlation index between both subsets, $DNm_{i,j}$ and $DNr_{i,j}$ are digital numbers of the moving window (second image) and reference subset (first image), μm and μr are the mean values of reference subsets and the moving window set, i and j are shifts between the central pixels of the reference subset and the moving window.

- For the central position C, L of the reference subset return that shift (the position of the moving window centre) where computed CI is the largest. In fig. 3(right), the centre of the moving window with highest CI is red and the centre of the corresponding reference frame in the first image in dark orange. Matching shift between them is noted as dC and dL – the cloud is in this example shifted two columns to the right and three lines to the bottom. If n_c and n_l are odd numbers, then the maximal possible shifts are $dC = (n_{c2} - n_{c1}) / 2$ and $dL = (n_{l2} - n_{l1}) / 2$.

Figure 3: Schema of area-based image matching.



4.1) Specifically, it is not explicitly explained over what range the sums in Eq. (1) are calculated, given that the 'search subset' and 'reference subset' are of different size. Is it implied that in the first image there is a fixed window of the size of the 'moving window' ($NC2 \times NL2$), centered at position C,L , and that the moving window in the second image is compared against this, with different shifts? In other words, is it implied that the 'reference subset' determines the size ($NC2 \times NL2$) of the moving window, and the 'search subset' merely limits the amount of the shift allowed? If the search window size determines the maximum shift ($13-7=6$ pixels), how is it possible to have shifts of over 10 pixels in Fig. 5?

The equation 1 was rewritten. Once a reference frame is selected in the first image, it is compared only to the underlying data from the second image. So here we compare data of the same size (7 by 7 pixels). In order not to make such a comparison for the whole dataset, we limit the area to search within the second dataset with so called search subset. With moving window analysis we compare all possible 7 by 7 pixels large datasets within the search subset with the reference subset. For each combination we compute CI. From the pixel having the highest CI and the central pixel of the search subset we can compute the shifts and later from them ACTH.

From this it follows, that the maximal shift depends on the size of the search and reference subset. But this is not, as you wrote, maximal 6 pixels – it is only a half of that – so maximal 3 pixels. But these pixels correspond to the image pyramid being processed. If we work on the pyramid, where each pixel is actually an average of 9 by 9 original pixels, this means that the actual shift (according to the original pixel size) can be $3 \cdot 9 = 27$ pixels!

4.2) Image pyramid method (p. 25629): It remains unclear how the image pyramids are used. Are the mentioned averages (3x3 and 9x9) calculated as moving averages, or are the image data regridded to coarser resolution? Do the mentioned window sizes (7x7 and 13x13) refer to the original resolution? If so, how is it possible to find decent correlations using a 7x7-moving window in a 9x9 averaged grid?

To produce a coarse image pyramid, the original data are always regridded, for instance:

- if we have first 270*540 pixel large original data
- we want to first average it within 3*3 pixel → the coarser pyramid has then 90*180 pixels
- regridding original to 9*9 pixels → the coarser pyramid has then 30*60 pixels

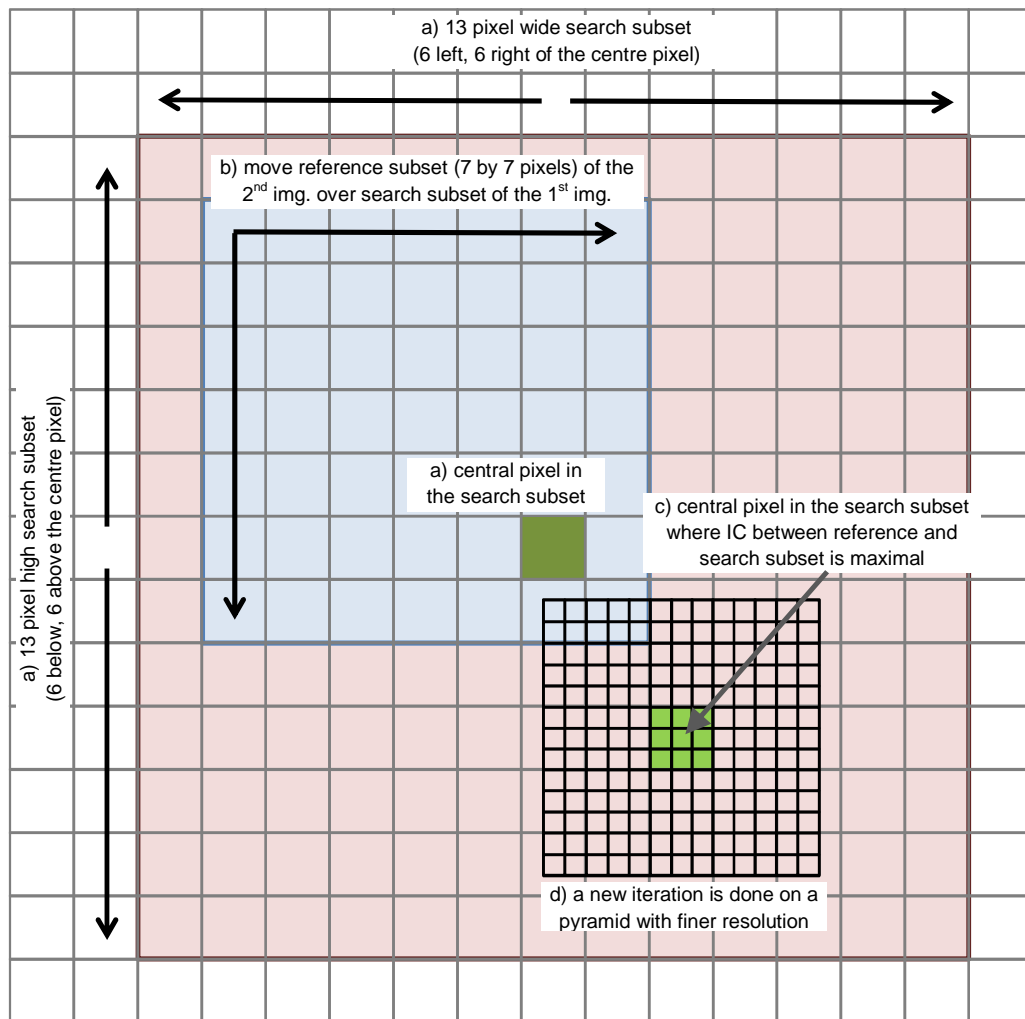
The mentioned search and reference subset thus always correspond to the pyramid being currently processed and not to the original pixels. The following text and figure are added:

We consider image pyramids as a multi-resolution representation of the original image (Anderson et al., 1984). Each higher pyramid is merely a regridded lower pyramid. The lowest pyramid is the original image. With each higher pyramid the resolution decreases for a chosen pyramid factor – in our case a factor of 3. Thus, the data of a higher pyramid are always averaged within 3x3 pixels large area of its lower pyramid. In our case we use three pyramids. For instance, if we had original data of 270 by 540 pixels we would aggregate them first to a pyramid of 90 by 180 pixels and in the following step to a pyramid of 30 by 60 pixels.

Shifts are first estimated over the image pyramid having the coarsest resolution. Search subset is defined (fig. 4, point a); the central points of the search subset coincide with the central points of the

reference subset. Image matching estimates the shift using moving window analysis (fig. 4, points b and c). These shifts are then refined on a lower pyramid. First they are multiplied by the pyramid factor and are regridded to the resolution of a lower pyramid (fig. 4, point d). These shifts then define new central points of each search subset in this pyramid. This procedure is repeated till the original data (the finest image pyramid) is processed. Such a scheme makes results more reliable and the computation is significantly faster. In the case CI between the compared datasets in a coarse pyramid was lower than 0.7 the estimated shifts were considered unreliable and set to 0. For all three levels of image pyramids the moving window was 7×7 pixels large and the search area 13×13 pixels large. Considering the geometry in the case study area, the size of the search subset and the chosen three image pyramids define the maximal ACTH to about 30 km.

Figure 4: Refinement of shifts using image pyramids.



4.3) If the maximum shift is limited in the method, it should be described what is the corresponding maximum ACTH.

We added a sentence in the end of section 3.2:

Considering the geometry in the case study area, the size of the search subset and the chosen three image pyramids define the maximal ACTH to about 30 km.

5) Section 4: It is not explained how the ash is generally distinguished from meteorological clouds (although BTM is mentioned). Is there an automatic process that can be used, or is the analysis made 'by the user'? In some parts of the discussion it seems that ACTH is confused with CTH; for example, is the data in Fig. 7 for ash contaminated pixels only (as implied in the text), or for all clouds?

We are mainly interested into the ash clouds but the method works just as good also on meteorological clouds. It is obvious that the ACTH will be faster computed if ash cloud is first masked. But the whole procedure takes only about 5 min, thus we computed ACTH for all the MODIS data that cover the area of interest. But for the Fig. 7 we have compared only the ash cloud heights with radar measurements. Ash detection is for this eruption a little bit tricky, because in the first phase of the eruption a lot of water was injected into the atmosphere. Thus we combine BTM with visual tracking of the plume to manually mask the ash cloud extent.

6) Section 5: It would be useful to discuss the cloud top wind speeds associated with the interpolation between the two SEVIRI images, and in connection to the column shifts (Fig. 5c).

We added the following text into the case study section (describing former fig.5, now fig. 7):

Column shifts are in the case study of lower importance for parallax estimation, but they are highly correlated to the wind velocity. The shifts shown in fig. 7 c–d correspond only to the SEVIRI data retrieved before MODIS retrieval. For an estimate of the wind velocity, the SEVIRI data after MODIS retrieval are needed. We do not show them here, but in the case study, the column shifts between both SEVIRI images can reach over 20 pixels. This corresponds to the velocity of over 80 km/h. As the wind direction was almost perpendicular to the SEVIRI line of sight, such a velocity does not significantly impact the ACTH estimation. However, if the wind had turned even more due south, the cloud advection would have been a major source of error in the case study.

Technical corrections

p. 25618, L25: 'restricted to their exceptional spatially and temporal availability'; Do you mean 'restricted to their specific spatial and temporal availability' ?

No, we really consider ground observations as exceptions because their measurements are spatially sparse distributed.

p. 25621, L1: 'Additional inaccuracy brings the instability of the temperature profile near the tropopause'; The sentence is unclear. Do you mean 'Additional inaccuracy is caused by the instability of the temperature profile near the tropopause' ?

yes, corrected

p. 25621, L13: 'currently launched'; Do you mean 'recently launched' ?

yes, corrected

p. 25622, L21: It is unclear to whom 'They' refers to. Do you mean 'O'Hara and Barnes showed that...' ?

yes, sentences are joined to make it clearer

p. 25629, L9: 'generate' -> 'generates'

corrected

p. 25631, L7: 'Island' -> 'Iceland'

corrected

p. 25631, L26: 'rise' -> 'rises'

yes, corrected

p. 25632, L28: 'Spatial distribution of CI...' I suggest rephrasing this sentence.

Changed to: "CI influences also the spatial distribution of shifts between both datasets in the column (Fig. 5 c) and line direction (Fig. 5 d)."

p. 25636, L20: What is meant by 'manual selection' ? Does this mean that the horizontal parallax is manually estimated from the images?

No, we have also manually selected some points to compare validate results of automatic image matching → this sentence is not so important and as it might cause confusion, we have deleted it.

p. 25637, L1: 'The ACTH error...' I suggest rephrasing this sentence.

Changed to: "The ACTH error coefficient correlates the ACTH error with the coordinate error of the matching pixel is false for 1 km."

p. 25653, Fig. 6: Reference to panel (b) is missing from the caption.

corrected

Monitoring volcanic ash cloud top height through simultaneous retrieval of optical data from polar orbiting and geostationary satellites

K. Zakšek¹², M. Hort¹, J. Zaletelj²³ and B. Langmann¹

[1]{Institute of Geophysics, University of Hamburg, Hamburg, Germany}

[2]{Centre of Excellence Space-SI, Ljubljana, Slovenia}

[3]{Faculty of Electrical Engineering, University of Ljubljana, Ljubljana, Slovenia}

Correspondence to: K. Zakšek (klemen.zaksek@zmaw.de)

Abstract

Volcanic ash cloud top height (ACTH) can be monitored on the global level using satellite remote sensing. Here we propose a photogrammetric method based on the parallax between data retrieved from geostationary and polar orbiting satellites to overcome some limitations of the existing methods of ACTH retrieval. SEVIRI HRV band and MODIS band 1 are a good choice because of their high resolution. The procedure works well if the data from both satellites are retrieved nearly simultaneously. MODIS does not retrieve the data at exactly the same time as SEVIRI. To compensate for advection we use two sequential SEVIRI images (one before and one after the MODIS retrieval) and interpolate the cloud position from SEVIRI data to the time of MODIS retrieval. The proposed method was tested for the case of the Eyjafjallajökull eruption in April 2010. The parallax between MODIS and SEVIRI data can reach over 30 km which implies ACTH of more than 12 km in the beginning of the eruption. In the end of April eruption ACTH of 3–4 km is observed. The accuracy of ACTH was estimated to be 0.6 km.

1 Introduction

Volcanic ash cloud top height (ACTH) is an important parameter in aviation route planning (Sparks, 1997) as well as in various volcanological models for estimating volcano's mass eruption rate (Mastin et al., 2009; Stohl et al., 2011). ACTH can be estimated using pilot reports, ground based, air-borne, and space-borne measurements. Ash clouds have been observed from the ground by weather radar in a number of instances, e.g. Rose et al. (1995), Lacasse et al. (2004). During the last couple of years observations of volcanic ash by ground lidar, eg. Gasteiger et al. (2011) or Hervo et al. (2012) received increasing attention. Although these are excellent tools, all ground based measurements are, however, restricted to their exceptional spatially and temporal availability.

Compared to ground or airborne based observations satellite remote sensing of ACTH has the great advantage of being available all the time. Geostationary satellites provide even temporal resolution of some minutes. The most reliable data are retrieved using active instruments like space-borne lidar (e.g. CALIOP, see section 2). However, only one such instrument is operating nowadays making it unsuitable for operational monitoring of volcanic plumes because of the long revisit time. A more

common method is based on the measurements of cloud brightness temperature, cloud emissivity, and atmospheric temperature profile. Because of the difficulties obtaining all parameters accurately, this method can lead to considerable ACTH errors. Improvements can be made using radiative transfer models as in e.g. Stohl et al. (2011). As another alternative we propose here a new solution for photogrammetric retrieval of ACTH.

In the following, we first give a further detailed introduction on available space-borne measurements in Sect. 2. Especially a detailed review on photogrammetric and stereoscopic ACTH measurements is presented in section 2.5 and 2.6. The proposed photogrammetric method is described in Sect. 3. Case study results are analysed in section 4. We finish with a discussion of the method's accuracy in section 5.

2 Existing methods of ACTH estimation

2.1 ACTH based on active sensors measurements

The Cloud-Aerosol Lidar with Orthogonal Polarization (CALIOP) is flying on the CALIPSO satellite (NASA, 2011). This instrument has a horizontal resolution of 333 m and vertical resolution between 30 and 180 m, depending on the distance to the ground. It has a revisit time of 16 days and a swath width of only one kilometre and performs only nadir measurements. CALIOP has already been used for volcanic ash cloud monitoring during, e.g. eruptions of Chaiten 2008 (Carn et al., 2009), Kasatochi 2008 (Karagulian et al., 2010) and Eyjafjallajökull 2010 (Stohl et al., 2011).

Another active instrument that might be used to determine ACTH height estimates is the Cloud Profiling Radar (CPR) aboard CloudSat (Colorado State University, 2011). It has lower vertical (240 m) and horizontal resolution (1700 m) than CALIOP, a revisit time of 16 days, and just like CALIOP provides only nadir measurements. CloudSat and CALIPSO fly in formation (same orbit with 15 s time delay), thus their results can be combined.

Because of the orbit characteristics the CALIOP and CPR instruments are prone to miss a volcanic eruption. Thus they are not appropriate for operational monitoring but are very useful for validation and supplementary information in case data are available.

2.2 ACTH based on brightness temperature

Satellite brightness temperature (BT) methods have been used several times to estimate ACTH (Oppenheimer, 1998; Prata and Grant, 2001; Tupper et al., 2004). This method compares BT retrieved from the ash cloud (normally utilizing the 11 μ m window channel) against the local vertical atmospheric temperature profile. The height at which the retrieved BT matches the atmospheric temperature profile is considered to be ACTH.

Several factors limit this technique (Oppenheimer, 1998). The first limitation is the assumption that the ash cloud top is in thermal equilibrium with the ambient air. If the ash cloud overshoots its thermally equilibrated level, or if the ash cloud still has sufficient energy to develop to higher altitudes (after the time of the satellite image), the BT-method does not work.

The second limitation is the assumption that the ash cloud emissivity equals 1. The actual emissivities are, however, poorly known. BT of thick ash clouds will under this assumption closely approximate

the true BT. But in the case of a dilute cloud the space-borne instrument will detect radiation from beneath the ash cloud, effectively lowering the heights.

Third, BT-methods also need an accurate atmospheric temperature profile. This profile depends mostly on season and latitude but even smaller variations can lead to significant ACTH errors. Additional inaccuracy is caused by the instability of the temperature profile near the tropopause (Prata and Grant, 2001). In case of the Eyjafjallajökull eruption, the tropopause is not higher than 10 km, thus the estimated ACTH of 9 km is already questionable. In tropical regions there are additional problems due to the so called double tropopause (Randel et al., 2007).

2.3 ACTH based on absorption by trace gasses

CO₂ absorption technique is a common method for estimating the cloud top height (Chang et al., 2010). It usually requires measurements at 11 μm as well as at 13–15 μm. The CO₂ absorption technique is based on the atmosphere becoming more opaque due to CO₂ absorption as the wavelength increases. This causes radiances obtained from spectral bands between 11 and 15 μm to be sensitive to a different layer of the atmosphere. The method yields the best accuracy for the upper troposphere. The problem is that the required bands are not available on many operational instruments (e.g. the Advanced Very High Resolution Radiometer (AVHRR), or even on the recently launched Visible Infrared Imager Radiometer Suite – VIIRS). This method has already been tested for ACTH estimation (Richards et al., 2006); isothermal regions and clouds at or near the tropopause cannot be retrieved using this algorithm because of the instability of the temperature profile near the tropopause. Another problem is the underestimation of ACTH since the method retrieves a radiative height (“height of the cloud centre”).

Height of (aerosol) clouds can be estimated from reflectance ratio measurements in the O₂ absorption A-band at 0.76 μm (Dubuisson et al., 2009; Preusker et al., 2007). The ratio is computed from a reflectance of a spectral band, strongly attenuated by O₂ absorption, and from the reflectance in a second spectral band with minimal attenuation. For a given surface reflectance, simple relations have been established between the reflectance ratio and the altitude of an aerosol layer as a function of atmospheric conditions and the geometry of observation. The method has been tested for POLDER (aboard ADEOS satellite) and MERIS (aboard ENVISAT satellite). The simulations show that the method is only accurate over dark surfaces when aerosol optical thickness is larger than 0.3. The same methodology is currently being tested also for ACTH estimation (ESA, 2011).

2.4 ACTH based on backward trajectories modelling

ACTH based on backward trajectories modelling correlates cloud movement with atmospheric winds (Eckhardt et al., 2008; Oppenheimer, 1998; Tupper et al., 2004). This method takes advantage of vertical wind profiles measurements – the horizontal wind component at any given altitude is usually unique in its combination of direction and speed. Therefore, airborne ash moves in this direction and with the speed of the prevailing wind. If the direction and speed of the airborne ash is determined from the satellite measurements, an estimate of ACTH is possible by matching the cloud movement with the corresponding wind movement. The method usually applies low spatial resolution satellite instruments with revisit time of about 12 hours as for instance Infrared Atmospheric Sounding Interferometer – IASI (Klüser et al., 2013). In general any kind of instruments can be used as long as they provide the data required by the model. It is the model that "moves" the detected ash cloud

back to its source, thus the quality of the model and meteorological data (wind velocity and direction as a function of height) are of highest importance. ACTH based on shadow lengths and photogrammetry

A trigonometric way of estimating ACTH is measuring the ash cloud shadow lengths (Glaze et al., 1989; Prata and Grant, 2001) on daytime images. The processing is more difficult if the method is used over rough terrain; as in this case the terrain elevation has to be considered. More important, the value of the shadow lengths usually corresponds to the margins of clouds, rather than their highest central points. To measure the top of the cloud height, the sun should be close to the horizon. But a large zenith angle has a consequence of low contrast, thus the shade mask is unreliable. A possible improvement is the combination of shadow length and temperature determinations using a photogrammetric study (Glaze et al., 1999; O'Hara and Barnes, 2012); they showed that the shadow technique alone systematically underestimates the ash cloud height by up to 30%.

2.5 ACTH based on stereoscopy

Parallax shifts of meteorological clouds or volcanic ash clouds are not obvious to many satellite data users because they mostly use imagery from a single satellite. However, when data from two different satellites are compared, the parallax shift becomes obvious – it is larger for higher clouds and plumes. Although proposed already before (Ondrejka and Conover, 1966) it was Hasler (1981) and Hasler et al. (1983) who drew attention to this by using two geostationary satellites (GOES) for stereoscopic measurements of cloud-top heights. Stereoscopy from geostationary satellites was also used for monitoring cumulonimbus clouds (Hasler et al., 1991), for research on convective clouds (Fujita, 1982; Mack et al., 1983), and for developing climatologic cloud monitoring systems (Wylie and Menzel, 1989). Because of the malfunction on GOES 6 the development in this field stopped until GOES 8 and GOES 9 were launched (Wylie et al., 1998).

In the studies listed above the cloud top was determined from a pair of GOES satellites. Seiz et al. (2007) used Meteosat images to retrieve cloud heights. The Meteosat-5/-8 HRV and Meteosat-5/-7 combination were tested. The resulting accuracy is about 1000 m which is worse than the estimated accuracy by GOES – which is 500 m (Hasler et al., 1983). The combination of Meteosat-5/-8 TIR data was used also for the eruption of Karthala (November 2005); Carboni et al. (2008) estimated the ACTH to be between 11 and 15 km above sea level.

An alternative to a pair of geostationary satellites are instruments with multi-angle observation possibilities. Prata and Turner (1997) proposed an algorithm for determining cloud heights based on the ATSR (aboard ERS satellites) forward and nadir views of clouds. The method has an accuracy of approximately 1000 m. It was used to determine ACTH for the Mt. Ruapehu eruption in 1996. Data were retrieved from ATSR-2. The heights on 8 July were about 8000 m for downwind points, and 5500 m for points near to the vent. Muller et al. (2007) showed that ATSR-2 cloud-top heights depend on the wavelengths used in the stereoscopy. They proposed that a combination of visible and thermal bands could yield information on multi-layer clouds. In addition Along Track Scanning Radiometer (ATSR) was used also for cloud detection in polar regions (Cawkwell et al., 2001).

In 1999 the Terra satellite was launched. Aboard are among other instruments the instruments Advanced Spaceborne Thermal Emission and Reflection Radiometer (ASTER) and Multi-angle Imaging

Spectro Radiometer (MISR). Both are capable of stereoscopic height measurements. Comparing different instruments it was shown that ASTER stereo cloud top heights are on average 1000 m higher than Moderate-resolution Imaging Spectroradiometer (MODIS) BT heights (Genkova et al., 2007). Unfortunately ASTER has only a 60 km wide swath and thus a long revisit time.

In the case of MISR, the revisit time is shorter (9 days, swath width of 360 km), thus it is more appropriate for use in volcanology. MISR was utilized to retrieve ACTH, optical depth, type, and shape of the finest particles of two highly explosive eruptions occurring on Mount Etna in 2001 and 2002 (Scollo et al., 2010, 2012). For Eyjafjallajökull eruption in 2010 it was also used to validate model estimated ACTH (Stohl et al., 2011) and plume particle-type characteristics (Kahn and Limbacher, 2012).

An interesting study was the use of the infrared spectral imaging radiometer that flew as part of mission STS-85 on the space shuttle Columbia in 1997 (Lancaster et al., 2003). A method for computing cloud-top height with a precision of 620 m based on multispectral stereo measurements was developed. The study is interesting because the results are compared with coincident direct laser ranging measurements from the shuttle laser altimeter (the laser altimeter mean heights were about 100 m lower). Another study using the same datasets (Manizade et al., 2006) showed that the accuracy of the height can be improved if the data are first segmented according to brightness temperature.

The combination of two different instruments, one aboard a satellite in geostationary and the other aboard a polar orbiter has also been suggested but never really exploited (Hasler et al., 1983). With several new instruments being in orbit since 1983 this combination offers new exciting possibilities that are detailed in the following section.

3 Proposed method of ACTH based on a parallax

The proposed method estimates ACTH based on the parallax of the data retrieved nearly simultaneously by two instruments. Fig. 1 shows the principle of the method: satellites in the polar and geostationary orbit do not observe an ash cloud at the same viewing angle. This causes parallax when comparing both images. The parallax depends on the differences in the viewing geometry and the height of the ash cloud. As the viewing geometry is defined by the coordinates of the retrieved data and the coordinates of both satellites it is easy to retrieve ACTH.

In our case study (Eyjafjallajökull eruption in April 2010; see section 4) we use a combination of MODIS aboard Terra and Aqua satellites (polar orbit) and Spinning Enhanced Visible and InfraRed Imager (SEVIRI) aboard Meteosat Second Generation 2 (MSG2) satellite in a geostationary orbit. Both instruments are multispectral but we limit the scope of this study to data from the visible spectrum allowing for ACTH estimations only during the day. The reason for this limitation is the spatial resolution of the retrieved data. The resolution has (besides parallax) the largest influence on the photogrammetrically estimated ACTH. HRV band of SEVIRI has a nominal resolution of 1000 m (in nadir) and MODIS bands 1 and 2 have nominal resolution of 250 m (in nadir; we used only band 1). These two resolutions are significantly higher than the resolutions of the accompanying thermal bands (3000 m for SEVIRI and 1000 m for MODIS).

The proposed method of ACTH estimation consists of three main steps. In the first step we aggregate MODIS data to SEVIRI spatial grid. The second step is automatic image matching. In the third step,

lines of sight connecting observed points of both satellites are generated; the intersection points of SEVIRI and MODIS lines of sight are then used to estimate ACTH.

3.1 Data pre-processing

To be able to perform automatic image matching it is necessary to pre-process data so that MODIS and SEVIRI datasets are comparable. In the previous retrievals of meteorologic cloud top height (Hasler, 1981) both images from GOES were projected to a standard map projection. All such transformations usually decrease the accuracy of the results. For the case study presented in section 4 SEVIRI with its poor spatial resolution is the parameter that limits the accuracy of the results, thus we decided to leave SEVIRI data in its own grid system. MODIS data have much better spatial resolution, thus they can be projected to the SEVIRI grid system without a significant influence on the resulting accuracy. The SEVIRI grid system is a normal geostationary projection, known also as near-side general vertical perspective projection. Therefore, the easiest way to transform a MODIS image to the SEVIRI grid is using the just mentioned map projection. The MSG2 satellite's position is, however, not stable. The satellite might change its position even for a hundred kilometres. Such changes in the satellite's position might lead into a positional error of the order of one pixel. Therefore, we prefer not to use a map projection to generate MODIS dataset in the SEVIRI grid system, but an alternative procedure (example in Fig. 2):

- Estimate, which MODIS pixels contribute to each SEVIRI pixels.
- Estimate the distance of each MODIS pixel from the corresponding SEVIRI pixel centre.
- Convert these distances to weights considering the SEVIRI point spread function (Deneke and Roebeling, 2010).
- Normalize the weights in such a way that their sum equals one for each SEVIRI pixel.
- To get the final MODIS based dataset in the SEVIRI grid, multiply all MODIS pixels with their weights and sum these values for each pixel of SEVIRI's grid.

3.2 Image matching

The goal of the satellite image matching step (called also image-to-image cross-correlation) is to accurately identify point pairs between two satellite images. This might be difficult if the images are not retrieved by the same instrument. The problem involves different resolutions, different viewing geometries, and different instruments response functions. In addition, the appearance of the same object in two different images might contain a large illumination variation, and thus the local descriptors of the same feature point are different. A number of automatic image matching approaches have been proposed to solve these issues. The methods can be categorised as area-based or feature-based methods (Evans, 2009; Goncalves et al., 2011; Hasan et al., 2010; Huo et al., 2012; Teke and Temizel, 2010).

Scale-invariant feature transform (SIFT) (Goncalves et al., 2011) and speeded-up robust features (SURF) (Evans, 2009) are becoming popular feature-based methods for camera image registration due to scale and rotation invariance of the detector and the distinctiveness of the descriptor. Simple

matching based on Euclidean difference between SURF descriptors is not sufficient. Several authors have proposed geometrical constraints such as scale and orientation restriction (Teke and Temizel, 2010) to improve the number of correct matches for remote sensing images. Our experiments proved that this was not enough in order to obtain a sufficient number of correct matches. We thus applied a more strict location relationship among neighbouring feature points, which allows only for small local position errors within a global affine transformation. Rather than using a single global mapping function for registration, we use local image patches, which are registered using affine model. Further experiments showed that it is possible to find matching features on the volcanic ash cloud. The problem is that only the small number of points is selected for further processing. In addition, it is difficult to control, which features are really chosen – we cannot be sure that the chosen features represent the highest parts of the volcanic ash cloud.

Although the feature-based image matching (SURF) performs good (results correspond well to results of manual points selection), we have tested also the area based image matching method. Such an approach allows the detection of more pixel pairs than the SURF based method. Many other approaches were used in previous studies (Hasler et al., 1991; Löfdahl, 2010; Ramapriyan et al., 1986; Scambos et al., 1992; Wu et al., 2012), some of which are based on the frequency domain and some on the image domain. As pointed out by Prata and Turner (1997), the frequency domain methods based on the fast Fourier transform makes sense only when working with large images. Within this study we were not comparing whole images but just parts of it using a moving window analysis. This was necessary as the case study area (see section 4) is large; in such a large area the clouds do not necessarily behave the same in all parts of the image. Thus it is necessary to determine local shifts by a moving window analysis. We used the same procedure as already described by e.g. Scambos et al. (1992) or Prata and Turner (1997). The method contains the following steps:

- Based on the pixel being currently processed (with image coordinates C, L) select a reference subset (with a number of columns n_{c1} and a number of lines n_{l1}) of the first image. This is shown in fig. 3 (left): pixel C, L is in red, the reference frame is yellow.
- In the second image select a search subset (with a number of columns $n_{c2} > n_{c1}$ and a number of lines $n_{l2} > n_{l1}$) that is centred over the pixel having the same image coordinates (C, L). This step merely reduces the possible extent of data subset from both images to be compared. Thus, it is theoretically not necessary but it reduces the computing time. The size of this search subset should be large enough to detect the largest expected shifts. Fig. 3 (right) shows the search subset (light orange) in the second image centred at the pixel C, L . (dark orange).
- Within the search subset define a moving window (with a number of columns n_{c1} and a number of lines n_{l1} – as large as the reference subset in the first image). The moving window is in fig. 3 (right) in yellow.
- Move this window across the search subset and for each possible shift of the moving window compute the normalized cross-covariance correlation C between the reference subset of the first image and the moving window from the second image (Eq. 1):

$$CI = \frac{\sum_{i=1-n_{c1}/2, j=1-n_{l1}/2}^{i=n_{c1}/2-1, j=n_{l1}/2-1} (DNr_{i,j} - \mu r) \cdot (DNm_{i,j} - \mu s)}{\sqrt{\sum_{i=1-n_{c1}/2, j=1-n_{l1}/2}^{i=n_{c1}/2-1, j=n_{l1}/2-1} (DNr_{i,j} - \mu r)^2} \cdot \sqrt{\sum_{i=1-n_{c1}/2, j=1-n_{l1}/2}^{i=n_{c1}/2-1, j=n_{l1}/2-1} (DNm_{i,j} - \mu s)^2}}, \quad (1)$$

where CI is the correlation index between both subsets, $DNm_{i,j}$ and $DNr_{i,j}$ are digital numbers of the moving window (second image) and reference subset (first image), μm and μr are the mean values of reference subsets and the moving window set, i and j are shifts between the central pixels of the reference subset and the moving window.

- For the central position C , L of the reference subset return that shift (the position of the moving window centre) where computed CI is the largest. In fig. 3(right), the centre of the moving window with highest CI is red and the centre of the corresponding reference frame in the first image in dark orange. Matching shift between them is noted as dC and dL – the cloud is in this example shifted two columns to the right and three lines to the bottom. If n_c and n_l are odd numbers, then the maximal possible shifts are $dC = (n_{c2} - n_{c1}) / 2$ and $dL = (n_{l2} - n_{l1}) / 2$.

The use of image matching is restricted to an estimation of image shifts between a pair of images. The shifts can be used to calculate those image coordinates in the second image that correspond to the points of the first image. In the proposed procedure of the ACTH estimate three images are always used: one MODIS, a SEVIRI image acquired just before, and a SEVIRI image acquired just after the MODIS image was retrieved. Therefore, image matching has to run twice to find matching points in all three images.

Results of image matching depend on the size of the search area and moving window. A large moving window can detect large but fail to detect small features. In contrast, a small moving window detects small features but generates a lot of noise in the results. The appropriate optimization is image matching over image pyramids. We consider image pyramids as a multi-resolution representation of the original image (Anderson et al., 1984). Each higher pyramid is merely a regridded lower pyramid. The lowest pyramid is the original image. With each higher pyramid the resolution decreases for a chosen pyramid factor – in our case a factor of 3. Thus, the data of a higher pyramid are always averaged within 3×3 pixels large area of its lower pyramid. In our case we use three pyramids. For instance, if we had original data of 270 by 540 pixels we would aggregate them first to a pyramid of 90 by 180 pixels and in the following step to a pyramid of 30 by 60 pixels.

Shifts are first estimated over the image pyramid having the coarsest resolution. Search subset is defined (fig. 4, point a); the central points of the search subset coincide with the central points of the reference subset. Image matching estimates the shift using moving window analysis (fig. 4, points b and c). These shifts are then refined on a lower pyramid. First they are multiplied by the pyramid factor and are regridded to the resolution of a lower pyramid (fig. 4, point d). These shifts then define new central points of each search subset in this pyramid. This procedure is repeated till the original data (the finest image pyramid) is processed. Such a scheme makes results more reliable and the computation is significantly faster. In the case CI between the compared datasets in a coarse

pyramid was lower than 0.7 the estimated shifts were considered unreliable and set to 0. For all three levels of image pyramids the moving window was 7×7 pixels large and the search area 13×13 pixels large. Considering the geometry in the case study area, the size of the search subset and the chosen three image pyramids define the maximal ACTH to about 30 km. Intersection of lines of sight for ACTH estimation

3.3 Intersection of lines of sight for ACTH estimation

After the triple of the corresponding image coordinates (from MODIS and both SEVIRI images) is known it is easy to compute their coordinates in a global coordinate system. The data required for the estimate of the longitude and latitude is usually part of the satellite dataset or can be obtained from their metadata. Also the satellite's ephemerides are usually a part of the metadata, which allows computing the satellite's position at the time of the data retrieval. Having these data it is would be possible to estimate ACTH following Prata and Turner (1997) from appropriate zenith angles. Here we propose another solution based on vector algebra.

- The first step is conversion of all available coordinates into a geocentric Cartesian coordinate system (see Appendix A).
- The effect of possible advection of the eruption cloud between the MODIS and the SEVIRI images is considered for each pixel triple: the coordinates of a virtual SEVIRI pixel are interpolated from position of both SEVIRI pixels to the time of MODIS retrieval.
- Define parametric equations of 3D lines connecting coordinates of the virtual SEVIRI pixels with the position of the MSG2 satellite ("SEVIRI lines") and corresponding lines connecting coordinates of the MODIS pixels with the position of the Terra/Aqua satellite ("MODIS lines").
- The solution of the following linear system gives intersection of such a line pair:

$$\begin{bmatrix} x \\ y \\ z \end{bmatrix}_M + t_M \cdot \begin{bmatrix} v_x \\ v_y \\ v_z \end{bmatrix}_M = \begin{bmatrix} x \\ y \\ z \end{bmatrix}_S + t_S \cdot \begin{bmatrix} v_x \\ v_y \\ v_z \end{bmatrix}_S, \quad (2)$$

where $[x, y, z]_M$ and $[x, y, z]_S$ are the positions of the MODIS aboard Terra/Aqua and SEVIRI aboard MSG2., $[v_x, v_y, v_z]_M$ and $[v_x, v_y, v_z]_S$ are direction vectors of MODIS and SEVIRI lines, t_M and t_S are the unknowns defining the point of intersection.

- The system in Eq. (2) is over determined, thus it can be solved by a least-square technique. The geocentric Cartesian coordinates of the intersection are then converted back to the geographic coordinate system: longitude, latitude, height above ellipsoid – i.e. ACTH (see Appendix A).

MODIS and SEVIRI lines never intersect because the data are not continuous but discrete pixels. The lines rather pass each other. Thus the Eq. (2) does not search for the real intersection but for the pair of closest points on the corresponding lines. ACTH can then be estimated from one of these two

points or as their average. The advantage of this ACTH estimate compared to the solution from zenith angles (Prata and Turner, 1997) is the possibility to estimate the intersection quality. It can be described by the distance between MODIS and SEVIRI lines; if it is small, the accuracy of ACTH is high. In the following, we use the expression “intersection distance” to express this value.

4 Case study: eruption of Eyjafjallajökull in April 2010

An explosive eruption under the Eyjafjallajökull glacier on Iceland started on April 14th 2010. The interaction of magma and melted water amplified the explosive activity which resulted into emissions of fine ash and volcanic gas into the atmosphere (Gudmundsson et al., 2010). Intense eruptive activity continued for five days. During this period prevailing meteorological conditions resulted in ash transport directly towards Europe (Fig. 5). The eruption strength increased again in May 2010.

In this case study we focus on the eruption period Apr. 15th–19th. The eruption featured an initially phreato-magmatic phase followed by a magmatic phase (Gudmundsson et al., 2010). However, volcanic eruptions undergo different phases of activity even during short periods of time in the order of seconds to minutes (Scharff et al., 2012). This can be seen in Fig. 6 which presents brightness difference temperature (BTD) from SEVIRI bands 9 and 10 with negative BTD being an indicator of ash presence in the atmosphere (Prata, 1989). The reddish coloured plume over the North Sea spreading towards Denmark is airborne ash. On its Western-end it is covered by a dark blue coloured cloud that is not recognized as airborne ash. BTD for this dark blue coloured cloud exceed +10 K being indicative of a meteorological cloud. However, analysis of the animated data shows, that this blue coloured plume is also of volcanic origin. It spreads from Eyjafjallajökull across the North Atlantic and the North Sea and then it turns to Northern France. During the phreato-magmatic eruption more water is injected into the atmosphere compared to a regular eruption. As the eruption cloud rises and cools, the water starts to condensate and eventually will form ice. In this case, condensation and ice formation are certainly enhanced by ash, which serves as nuclei for water and ice condensation. Therefore, one can assume from BTD that the blue plume in Fig. 6 consist not only of ice, but of ice with ash. This blue plume is located higher than the plume in red. Because of this height differences the dispersion of both plumes is different. The red part moves first to the east and eventually to the south-east and the blue part to the south-west.

Fig. 7 shows an example for Apr. 17th at 13:15 UTC. SEVIRI image (Fig. 7 a) retrieved some minutes before the MODIS image covers the whole study area. South of 60 °N a large area of meteorological clouds covers the area of the North Atlantic, Northern Ireland and Scotland. These clouds reach height from 4 km to over 9 km. After the initial part of the eruption they moved over North Atlantic covering Iceland on the evening of Apr. 15th. This restricted monitoring of volcanic ash over Iceland by thermal remote sensing. Once they uncovered Iceland in the beginning of Apr. 17th a small ash cloud could be observed again. This can be seen in Fig. 7 (a) stretching from Iceland first to the south and then turning to the east. Note that the majority of the ash cloud is positioned north of 60°N. Furthermore, a very high cloud can be observed over the North Sea. From the visible SEVIRI image (Fig. 7 a) it does not seem thick compared to the previously discussed meteorological clouds. Its origin is difficult to determine. BTD is highly positive, indicating a meteorological cloud. However analysis of the animation shows that the cloud first appeared above Scotland. As it remained moving in the similar direction as the first ash cloud reaching Scotland, we assume that this is also an ice cloud originating from the volcano that was for some time “hidden” by higher clouds.

Fig. 7 (b) shows the cross-correlation index (CI ; Eq. 1) between the shown SEVIRI image (Fig. 7 a) and corresponding MODIS image retrieved at 13:15 UTC. As expected it is very high along the coastal areas having large contrast between the land and the sea. The lowest CI is within large land areas and the open sea not covered by clouds. Similar characteristic can be observed in cloudy areas – where clouds contain some edges and texture CI is high as well. CI influences also the spatial distribution of shifts between both datasets in the column (Fig. 7 c) and line direction (Fig. 7 d). Where CI is low, sudden changes of shifts are possible. Especially shifts in the line direction are influenced mostly by the parallax between MODIS and SEVIRI data (Fig. 7 e). The highest parts of the clouds have parallax larger than 30 km. This is a shift of MODIS data for about 10 pixels to the north in the case study area. Such a shift can be easily observed even by visual comparison of MODIS and SEVIRI data. Column shifts are in the case study of lower importance for parallax estimation, but they are highly correlated to the wind velocity. The shifts shown in fig. 7 c–d correspond only to the SEVIRI data retrieved before MODIS retrieval. For an estimate of the wind velocity, the SEVIRI data after MODIS retrieval are needed. We do not show them here, but in the case study, the column shifts between both SEVIRI images can reach over 20 pixels. This corresponds to the velocity of over 80 km/h. As the wind direction was almost perpendicular to the SEVIRI line of sight, such a velocity does not significantly impact the ACTH estimation. However, if the wind had turned even more due south, the cloud advection would have been a major source of error in the case study.

Fig. 7 (f) shows the intersection distance between MODIS and SEVIRI lines of sight (solution of Eq. 2 using least-square technique); these values can reach distances of some kilometres. Assuming that the accuracy of image matching is a half of pixel then this intersection distance should not exceed this value for a reliable solution. Here we are interested only in the north-south direction because this is the direction in which the parallax mainly extends. The pixel size in the north-south direction is about 3 km in the case study area, thus the intersection distance should here not be larger than 1.5 km. Therefore, many pixels with estimated ACTH (Fig. 7 g) are not reliable. It is possible to filter all these pixels (Fig. 7 h) but enough pixels are left so that a good impression of the cloud topography is possible. The highest pixels represent clouds over the North Sea that reach even heights over 10 km. Another signal shows a meteorological cloud spreading west to east just south of 60°N. As mentioned before this is the remaining of the cloud that was covering the whole area of Iceland from late Apr. 15th to early Apr. 17th. Its height is mostly between 6 and 9 km. Just north of it, an ash cloud stretching back to Iceland is positioned. It is much lower than the ash cloud was on the first day of eruption but the highest pixels still reach over 6 km.

Another example is shown for the first phase of the eruption on Apr. 15th (Fig. 8 a). The plume stretches from Iceland over North Sea north of Scotland in the direction of Norway. The plume can be easily detected directly from the visualised ACTH as it is much higher than the surroundings. The plume ACTH ranges mostly between 5 km and 8 km but some pixels reach even 12 km. The plume is, however, difficult to recognize a few days later on Apr. 19th as the eruption intensity has already decreased by that time (Fig. 8 b). The ash plume reaches over 3 km high (orange pixels south of Iceland) which is approximately as high as the surrounding clouds.

Aside from the spatial extent of the cloud it is also interesting to examine the temporal evolution of the ACTH. The analysis covers the ACTH of volcanic ash clouds within the area covering Iceland, North Sea, Ireland and UK (the extent shown in Fig. 7). Fig. 9 shows how the ACTH vertical distribution changes over the case study period (see Appendix B for the list of used datasets). Fig. 9 shows how many ash cloud pixels (in percent) are situated in each height class with 500 m vertical resolution.

The maximum ACTH values reached about 12 km which corresponds well to the estimation by Stohl et al. (2011). London VAAC reported higher ACTH of over 16 km (Fig. 5), but these values are probably exaggerated because of the air-traffic safety.

Fig. 9 contains also the ACTH estimations from ground radar measurements (see Fig. 5 in Marzano et al. (2011)). Both datasets show that ACTH tends to get lower over time as the eruption intensity decreases. It should be considered that the radar vertical resolution is about 2.5 km for the case study geometry. This is a reason that the radar data oscillate significantly. In addition, the radar data range is limited to 240 km away from the radar position, so most likely not more than 100 km from the volcano. See Fig. 1 in Marzano et al. (2011) to compare the radar range with our case study area shown in Fig. 7. Our measurements in Fig. 9 contain also data that are even 1000 km away from the volcano. The case study area was not restricted to the same vicinity of the volcano as by radar measurements. This is because too few satellite measurements are then available making the vertical distribution unreliable. Therefore, the ACTH distribution in Fig. 9 presents not only ACTH at the source, but also during long-range advection.

5 Discussion

The transport of volcanic ash in the atmosphere and its deposition on land and in the oceans is of significant importance for climate development (Langmann et al., 2010; Robock, 2000). A direct consequence of the airborne ash is usually a closure of the air space for air traffic. Thus it is very important to monitor the horizontal and vertical dispersion of volcanic ash during an eruption. The observations of the vertical ash dispersion are still limited to radar and lidar observations but more methods are available for monitoring the top of ash clouds. One of them is the method presented here. In the following we discuss its accuracy that depends on:

- ACTH itself,
- accuracy of image registration (image positional accuracy),
- accuracy of satellite's position,
- accuracy of image matching, and
- accuracy of the wind velocity.

The influence of ACTH itself on its accuracy can be ignored for satellite remote sensing. The ratio between ACTH and the satellite height above the Earth is too small to have a significant effect on the results. The accuracy of the satellite's position and positional accuracy of an image cannot be controlled by a user of remote sensing data. The position of a satellite is not a significant problem for the satellites in the geostationary orbit. It is more problematic for the satellites in the polar orbit because their position changes rapidly (some kilometres per second). The positional accuracy of an image has, however, always a major influence on results.

5.1 Accuracy of image matching and its influence on ACTH

The remaining sources of error in ACTH estimation are the accuracy of image matching and the accuracy of the wind velocity. These have already been discussed by Seiz et al. (2007). Their estimate of the height accuracy is based on the ratio between the base (to the Earth projected distance

between satellites) and height of the satellites. We did not follow their estimate because the heights of satellites used in the study are not the same (705 km for Aqua and Terra satellites carrying MODIS and almost 36,000 km for MSG2 satellite carrying SEVIRI). In addition, wind velocity is already integrated in our approach by using two sequential SEVIRI images.

Therefore, image matching is the only source of inaccuracy of the proposed method. It is more reliable if the compared images are made under similar conditions, for instance: the same time of acquisition and the same geometry between the instruments and observing surface is given. If the observing surface changes during the time period as both images were acquired, the image matching will likely fail. This limits monitoring of the ash plume at the vent using the presented approach; 15 min is a too long period to observe the rising ash cloud at the vent because it changes its form and its height significantly. Therefore, one might wonder why MSG1 data were not used in this study. MSG1 carries also SEVIRI just as MSG2, but since 2009 it functions in the rapid scan mode – it monitors only Europe at the 5 min interval. With a shorter retrieval interval the results would obviously be more robust. However, MSG1 is positioned approximately at 9 °E longitude and MSG2 at 0° E. This 9° of difference does not seem much, but Iceland in the case of MSG2 is already pushed to the edge of the visible hemisphere. In the case of MSG1 data, Iceland is just on the horizon, which increases the data spatial resolution and this lowers the ACTH accuracy.

In general the results of image matching between datasets acquired by two different instruments depend also on the used spectral bands. If the ash and meteorological clouds do not have similar reflectivity in MODIS and SEVIRI spectral bands, image matching is likely to fail. Here we use SEVIRI HRV band that covers a large part of visible and near infrared spectrum. Furthermore, we used MODIS band 1 that covers only “red” spectrum of the visible light. The comparison of both datasets has shown that the data covering clouds and volcanic ash are highly correlated, which justifies bands’ selection. In addition, different atmospheric path length of SEVIRI and MODIS measurements does not influence the results. For the sake of completeness, we here mention also the ability of image matching to detect also transparent clouds. This is usually not a problem if the underlying surface is homogenous. For instance, dark ocean surface is a suitable background. If the texture in the background varies significantly, the image matching will fail.

To estimate the accuracy of image matching analytically some simplifications are made: ignore Earth curvature (on the distance of the parallax below 40 km this leads into the height error of not more than 100 m), assume that MODIS looks into nadir, and consider merely a 2D space (meridian plane). These assumptions result into a simplified geometrical problem (Fig. 10 a); the error increases linearly with increasing error in parallax P ($\Delta\text{ACTH} = \Delta P \cdot \tan \alpha$). The satellite elevation angle α depends on the latitude (because of the simplification; it actually depends on the angular distance from the SEVIRI’s nadir). Fig. 10 (b) shows the relationship between the ACTH error coefficient and the latitude. The ACTH error coefficient correlates the ACTH error with the coordinate error of the matching pixel is false for 1 km. Fig. 10 shows that the error decreases with increasing latitude. In our case (assuming latitude of 60°) this coefficient equals to 0.4 km/km. If image matching makes a mistake of half of pixel to the North (this corresponds to 1.5 km in the north-south direction for the case study area), the ACTH error will be about 0.6 km.

The reliability of image matching can be estimated from the intersection distance between the MODIS and SEVIRI lines of sight. The reliability of the least square solution of the lines intersection is

large if the intersection distance between the lines of sight is close to zero. Mainly the north–south component is interesting in the case study area because the parallax between MODIS and SEVIRI extends approximately in this direction. East–west component of the intersection distance has almost no influence on ACTH, thus the intersection distance was projected to the north direction. These values are usually in the range of up to 1 km, which is less than half of pixel size for the study area. The intersection distance depends not only on the image matching accuracy but also on the accuracy of the satellite position and positional accuracy of the image data. This makes it suitable as a general accuracy estimate of the method.

5.2 Comparison with other methods

We compare our results with the plume height measured by MISR (Nelson et al., 2008). Wind corrected heights of the ash plume were obtained from the MISR Plume Height Project (<http://misr.jpl.nasa.gov/getData/accessData/MisrMinxPlumes/>). Fig. 11 shows the difference between our ACTH and MISR ACTH for Apr. 19th at 12:51 UTC, which are significant. One reason for the discrepancy may be vicinity of the vent; the northern part of the plume is probably still developing, it moves also vertically making the ACTH estimations of MISR as well as ours totally unreliable. In the southern part of the plume the difference seems more systematic. Our estimation is about 1 km higher than MISR ACTH. The reason for that most likely lies in the poor positional accuracy of SEVIRI data. After visual comparison we observed that Iceland seems to be shifted for a pixel when comparing MODIS and SEVIRI data. Such a shift was not observed in other parts of Europe (United Kingdom, or France). We conclude that the positional accuracy of SEVIRI data is not optimal, thus this inaccuracy propagates to ACTH (at least in the closest vicinity of Iceland).

We compare our results also with the standard MODIS cloud product MOD06_L2 based on the CO₂ absorption technique (Platnick et al., 2003). Its spatial resolution is about 5 km. The product estimates the top of the cloud height pressure and not geometrical height. To convert the pressure into the geometrical height we use atmospheric sounding data for the location of Tórshavn (Faroe Islands; 62.01° N, 6.76° W) on 15 April 2010 at 12:00 UTC. The time of the atmospheric sounding is not the same as the time of MODIS retrieval (11:35 UTC; see fig. 8a). The valid plume pixels seem in general to be higher in our results than in the MOD06_L2 product (fig. 12 a). The bias equals approximately 650 m.

The same sounding data are used also to estimate ACTH with the BT method (fig. 12 b). Because the measured temperature in the sounding data fluctuates, it is possible to apply this sounding only for the clouds that are between 4 km and 11 km. The ash plume was in this range but the clouds around it not, thus fig. 12 compares ACTH only the area of the ash plume. The results of the BT method have a bias of 2200 m compared to the proposed method. A bias larger than 1000 m was observed already in similar previous studies (Genkova et al., 2007). The reason for the biases is in the retrieval of a radiative height that does not estimate exactly the top of the cloud but the height of the “cloud centre”.

6 Conclusions

In the case study of the Eyjafjallajökull eruption in spring 2010 we applied the proposed method only to data collected in the visible spectrum, because of the high spatial resolution, but it can be used also with e.g. infrared spectra. New instruments with better characteristics will be available in the following years allowing application of our method. For instance, the third generation Meteosat

should provide also regional rapid scans every 2.5 min at a spatial resolution of 0.5 km in a visible band (0.6 μm) or 1.0 km in a thermal band (10.5 μm). Use of thermal bands will allow the application of the proposed method also during night-time.

In the future we plan to improve the accuracy of the image matching to the sub-pixel level. The accuracy of the current ACTH estimates is better than 0.6 km. With sub-pixel image matching the estimates of shifts could be enhanced to about 0.1–0.2 of a pixel size. This would increase the ACTH accuracy to 0.2 km or even better. To achieve appropriate results in image matching data pre-processing will require more effort: 1) use of Wallis filter to locally enhance contrast in the data and 2) additional corrections of image registration by using of vector data to improve the positional accuracy.

The greatest advantage of the proposed method to determine ACTH is its independence of physical assumptions. The method has a purely geometrical background, thus there is no need for any additional data (as for instance ash emissivity or atmospheric temperature profile). The geometrical solution is fast and it can be applied to any combination of a polar orbiting satellite and a geostationary satellite. The only requirement is that the temporal resolution of the geostationary satellite is high enough, that clouds in the size of the used moving window do not change their form significantly but just move to a new position. This allows correlating data retrieved from both orbits even if they were not retrieved at exactly the same time. The combination of geostationary and any polar orbiting instruments that have similar spectral bands can be used to measure ACTH a few times per day. It can be used as well for monitoring of meteorological clouds, volcanic plumes, mineral dust and vegetation fire plumes.

Acknowledgements

This research has been supported by grants from the German Science Foundation (DFG) number ZA659/1-1. The study was supported also through the Cluster of Excellence 'CliSAP' (EXC177), University of Hamburg, funded through DFG. The Centre of Excellence for Space Sciences and Technologies Space-SI is an operation partly financed by the European Union, European Regional Development Fund, and Republic of Slovenia, Ministry of Higher Education, Science and Technology.

The SEVIRI L1.5 data were obtained through the online archive of EUMETSAT images (Earth Observation Portal). The MODIS L1B data and cloud product were obtained through the online Data Pool at the NASA Land Processes Distributed Active Archive Center (LP DAAC), USGS/Earth Resources Observation and Science (EROS) Center, Sioux Falls, South Dakota (https://lpdaac.usgs.gov/get_data). The London VAAC data were obtained through personal communication with N. Gait and C. Tyson (UK Met Office). The radar data were obtained through personal communication with F. S. Marzano (Sapienza University of Rome). The MISR data were obtained through the online archive of MISR Plume Height Project (<http://mISR.jpl.nasa.gov/getData/accessData/MisrMinxPlumes/>). Atmospheric temperature profiles were obtained through the online archive Wyoming Weather Web of the University of Wyoming.

References

Anderson, C. H., Bergen, J. R., Burt, P. J. and Ogden, J. M.: Pyramid Methods in Image Processing, RCA Engineer, 29(6), 33–41, 1984.

Carboni, E., Grainger, R., Thomas, G., Poulsen, C., Siddans, R., Smith, A., Sayer, A. and Peters, D.: Volcanic plume characterization using satellite measurements in the visible and thermal infrared, in Second Workshop on Use of Remote Sensing Techniques for Monitoring Volcanoes and Seismogenic Areas, 2008. USEReST 2008., 2008.

Carn, S. A., Pallister, J. S., Lara, L., Ewert, J. W., Watt, S., Prata, A. J., Thomas, R. J. and Villarosa, G.: The Unexpected Awakening of Chaitén Volcano, Chile, *Eos Trans. AGU*, 90(24), P. 205, doi:200910.1029/2009EO240001, 2009.

Cawkwell, F. G. L., Bamber, J. L. and Muller, J. -P.: Determination of cloud top amount and altitude at high latitudes, *Geophys. Res. Lett.*, 28(9), PP. 1675–1678, doi:200110.1029/2000GL012684, 2001.

Chang, F.-L., Minnis, P., Lin, B., Khaiyer, M. M., Palikonda, R. and Spangenberg, D. A.: A modified method for inferring upper troposphere cloud top height using the GOES 12 imager 10.7 and 13.3 μm data, *J. Geophys. Res.*, 115(D6), D06208, doi:10.1029/2009JD012304, 2010.

Colorado State University: CloudSat, [online] Available from: <http://cloudsat.atmos.colostate.edu/> (Accessed 11 February 2011), 2011.

Deneke, H. M. and Roebling, R.: Downscaling of METEOSAT SEVIRI 0.6 and 0.8 micron channel radiances utilizing the high-resolution visible channel, *Atmos. Chem. Phys. Discuss.*, 10(4), 10707–10740, doi:10.5194/acpd-10-10707-2010, 2010.

Dubuisson, P., Frouin, R., Dessailly, D., Duforêt, L., Léon, J.-F., Voss, K. and Antoine, D.: Estimating the altitude of aerosol plumes over the ocean from reflectance ratio measurements in the O2 A-band, *Remote Sensing of Environment*, 113(9), 1899–1911, doi:10.1016/j.rse.2009.04.018, 2009.

Eckhardt, S., Prata, A. J., Seibert, P., Stebel, K. and Stohl, A.: Estimation of the vertical profile of sulfur dioxide injection into the atmosphere by a volcanic eruption using satellite column measurements and inverse transport modeling, *Atmos. Chem. Phys.*, 8(14), 3881–3897, doi:10.5194/acp-8-3881-2008, 2008.

ESA: Envisat keeping an eye on the Eyjafjallajökull volcano, [online] Available from: http://www.esa.int/esaEO/SEMW3NF098G_planet_0.html (Accessed 14 February 2011), 2011.

Evans, C.: Notes on the OpenSURF Library, [online] Available from: http://www.cs.bris.ac.uk/Publications/pub_master.jsp?id=2000970, 2009.

Fujita, T. T.: Principle of stereoscopic height computations and their applications to stratospheric cirrus over severe thunderstorms, *J. Meteor. Soc. Japan*, 60, 355–368, 1982.

Gasteiger, J., Groß, S., Freudenthaler, V. and Wiegner, M.: Volcanic ash from Iceland over Munich: mass concentration retrieved from ground-based remote sensing measurements, *Atmos. Chem. Phys.*, 11(5), 2209–2223, doi:10.5194/acp-11-2209-2011, 2011.

Genkova, I., Seiz, G., Zuidema, P., Zhao, G. and Di Girolamo, L.: Cloud top height comparisons from ASTER, MISR, and MODIS for trade wind cumuli, *Remote Sensing of Environment*, 107(1-2), 211–222, doi:10.1016/j.rse.2006.07.021, 2007.

Glaze, L. S., Francis, P. W., Self, S. and Rothery, D. A.: The 16 September 1986 eruption of Lascar volcano, north Chile: Satellite investigations, *Bull Volcanol*, 51(3), 149–160, doi:10.1007/BF01067952, 1989.

Glaze, L. S., Wilson, L. and Mougini-Mark, P. J.: Volcanic eruption plume top topography and heights as determined from photogrammetric analysis of satellite data, *J. Geophys. Res.*, 104(B2), PP. 2989–3001, doi:10.1029/1998JB900047, 1999.

Goncalves, H., Corte-Real, L. and Goncalves, J. A.: Automatic Image Registration Through Image Segmentation and SIFT, *Geoscience and Remote Sensing, IEEE Transactions on*, 49(7), 2589–2600, doi:10.1109/TGRS.2011.2109389, 2011.

Gudmundsson, M. T., Pedersen, R., Vogfjörð, K., Thorbjarnardóttir, B., Jakobsdóttir, S. and Roberts, M. J.: Eruptions of Eyjafjallajökull Volcano, Iceland, *Eos Trans. AGU*, 91(21), 190–191, doi:10.1029/2010EO210002, 2010.

Hasan, M., Jia, X., Robles-Kelly, A., Zhou, J. and Pickering, M. R.: Multi-spectral remote sensing image registration via spatial relationship analysis on sift keypoints, in *Geoscience and Remote Sensing Symposium (IGARSS), 2010 IEEE International*, pp. 1011–1014., 2010.

Hasler, A. F.: Stereographic Observations from Geosynchronous Satellites: An Important New Tool for the Atmospheric Sciences, *Bull Amer Met Soc*, 62(2), 194, doi:10.1175/1520-0477(1981)062<0194:SOFGSA>2.0.CO;2, 1981.

Hasler, A. F., Mack, R. and Negri, A.: Stereoscopic observations from meteorological satellites, *Advances in Space Research*, 2(6), 105–113, doi:10.1016/0273-1177(82)90130-2, 1983.

Hasler, A. F., Strong, J., Woodward, R. H. and Pierce, H.: Automatic Analysis of Stereoscopic Satellite Image Pairs for Determination of Cloud-Top Height and Structure, *J. Appl. Meteor.*, 30(3), 257–281, doi:10.1175/1520-0450(1991)030<0257:AAOSSI>2.0.CO;2, 1991.

Hervo, M., Quennehen, B., Kristiansen, N. I., Boulon, J., Stohl, A., Fréville, P., Pichon, J.-M., Picard, D., Labazuy, P., Gouhier, M., Roger, J.-C., et al.: Physical and optical properties of 2010 Eyjafjallajökull volcanic eruption aerosol: ground-based, Lidar and airborne measurements in France, *Atmos. Chem. Phys.*, 12(4), 1721–1736, doi:10.5194/acp-12-1721-2012, 2012.

Huo, C., Pan, C., Huo, L. and Zhou, Z.: Multilevel SIFT Matching for Large-Size VHR Image Registration, *Geoscience and Remote Sensing Letters, IEEE*, 9(2), 171–175, doi:10.1109/LGRS.2011.2163491, 2012.

Kahn, R. A. and Limbacher, J.: Eyjafjallajökull volcano plume particle-type characterization from space-based multi-angle imaging, *Atmospheric Chemistry and Physics Discussions*, 12(7), 17943–17986, doi:10.5194/acpd-12-17943-2012, 2012.

Karagulian, F., Clarisse, L., Clerbaux, C., Prata, A. J., Hurtmans, D. and Coheur, P. F.: Detection of volcanic SO₂, ash, and H₂SO₄ using the Infrared Atmospheric Sounding Interferometer (IASI), *J. Geophys. Res.*, 115(D2), D00L02, doi:10.1029/2009JD012786, 2010.

Klüser, L., Erbertseder, T. and Meyer-Arneke, J.: Observation of volcanic ash from Puyehue–Cordón Caulle with IASI, *Atmospheric Measurement Techniques*, 6(1), 35–46, doi:10.5194/amt-6-35-2013, 2013.

Lacasse, C., Karlsdóttir, Larsen, G., Soosalu, H., Rose, W. I. and Ernst, G. G. J.: Weather radar observations of the Hekla 2000 eruption cloud, Iceland, *Bulletin of Volcanology*, 66(5), 457–473, doi:10.1007/s00445-003-0329-3, 2004.

- Lancaster, R. S., Spinhirne, J. D. and Manizade, K. F.: Combined Infrared Stereo and Laser Ranging Cloud Measurements from Shuttle Mission STS-85, *J. Atmos. Oceanic Technol.*, 20(1), 67–78, doi:10.1175/1520-0426(2003)020<0067:CISALR>2.0.CO;2, 2003.
- Langmann, B., Zakšek, K., Hort, M. and Duggen, S.: Volcanic ash as fertiliser for the surface ocean, *Atmos. Chem. Phys.*, 10(8), 3891–3899, 2010.
- Löfdahl, M. G.: Evaluation of image-shift measurement algorithms for solar Shack-Hartmann wavefront sensors, *Astronomy and Astrophysics*, 524, 90, doi:DOI: 10.1051/0004-6361/201015331; eprintid: arXiv:1009.3401, 2010.
- Mack, R. A., Hasler, A. F. and Adler, R. F.: Thunderstorm Cloud Top Observations Using Satellite Stereoscropy, *Monthly Weather Review*, 111(10), 1949–1964, 1983.
- Manizade, K. F., Spinhirne, J. D. and Lancaster, R. S.: Stereo Cloud Heights From Multispectral IR Imagery via Region-of-Interest Segmentation, *IEEE Transactions on Geoscience and Remote Sensing*, 44(9), 2481–2491, doi:10.1109/TGRS.2006.873339, 2006.
- Marzano, F. S., Lamantea, M., Montopoli, M., Di Fabio, S. and Picciotti, E.: The Eyjafjöll explosive volcanic eruption from a microwave weather radar perspective, *Atmos. Chem. Phys.*, 11(18), 9503–9518, doi:10.5194/acp-11-9503-2011, 2011.
- Mastin, L. G., Guffanti, M., Servranckx, R., Webley, P., Barsotti, S., Dean, K., Durant, A., Ewert, J. W., Neri, A., Rose, W. I., Schneider, D., et al.: A multidisciplinary effort to assign realistic source parameters to models of volcanic ash-cloud transport and dispersion during eruptions, *Journal of Volcanology and Geothermal Research*, 186(1–2), 10–21, doi:10.1016/j.jvolgeores.2009.01.008, 2009.
- Muller, J.-P., Denis, M.-A., Dundas, R. D., Mitchell, K. L., Naud, C. and Mannstein, H.: Stereo cloud-top heights and cloud fraction retrieval from ATSR-2, *International Journal of Remote Sensing*, 28(9), 1921, doi:10.1080/01431160601030975, 2007.
- NASA: CALIPSO - Cloud-Aerosol Lidar and Infrared Pathfinder Satellite Observations, [online] Available from: <http://www-calipso.larc.nasa.gov/> (Accessed 11 February 2011), 2011.
- Nelson, D. L., Chen, Y., Kahn, R. A., Diner, D. J. and Mazzoni, D.: Example applications of the MISR IInteractive eXplorer (MINX) software tool to wildfire smoke plume analyses, vol. 7089, pp. 708909–708909–11, SPIE. [online] Available from: <http://proceedings.spiedigitallibrary.org/proceeding.aspx?articleid=1327788> (Accessed 19 September 2012), 2008.
- O’Hara, R. and Barnes, D.: A new shape from shading technique with application to Mars Express HRSC images, *ISPRS Journal of Photogrammetry and Remote Sensing*, 67, 27–34, doi:10.1016/j.isprsjprs.2011.07.004, 2012.
- Ondrejka, R. J. and Conover, J. H.: Note on the stereo interpretation of nimbus ii apt photography, *Monthly Weather Review*, 94(10) [online] Available from: <http://journals.ametsoc.org/doi/abs/10.1175/1520-0493%281966%29094%3C0611%3A%20NOTSIO%3E2.3.CO%3B2> (Accessed 17 February 2011), 1966.
- Oppenheimer, C.: Review article: Volcanological applications of meteorological satellites, *International Journal of Remote Sensing*, 19(15), 2829, doi:10.1080/014311698214307, 1998.

- Platnick, S., King, M. D., Ackerman, S. A., Menzel, W. P., Baum, B. A., Riedi, J. C. and Frey, R. A.: The MODIS cloud products: algorithms and examples from Terra, *IEEE Transactions on Geoscience and Remote Sensing*, 41(2), 459 – 473, doi:10.1109/TGRS.2002.808301, 2003.
- Prata, A. J.: Observations of volcanic ash clouds in the 10-12 micron window using AVHRR/2 data, [online] Available from: <http://adsabs.harvard.edu/abs/1989IJRS...10..751P> (Accessed 15 March 2010), 1989.
- Prata, A. J. and Grant, I. F.: Retrieval of microphysical and morphological properties of volcanic ash plumes from satellite data: Application to Mt Ruapehu, New Zealand, *Q.J Royal Met. Soc.*, 127(576), 2153–2179, doi:10.1002/qj.49712757615, 2001.
- Prata, A. J. and Turner, P. J.: Cloud-top height determination using ATSR data, *Remote Sensing of Environment*, 59(1), 1–13, doi:10.1016/S0034-4257(96)00071-5, 1997.
- Preusker, R., Fischer, J., Albert, P., Bennartz, R. and Schüller, L.: Cloud-top pressure retrieval using the oxygen A-band in the IRS-3 MOS - instrument, *International Journal of Remote Sensing*, 28(9), 1957, doi:10.1080/01431160600641632, 2007.
- Ramapriyan, H. K., Strong, J. P., Hung, Y. and Murray, C. W.: Automated Matching of Pairs of SIR-B Images for Elevation Mapping, *IEEE Transactions on Geoscience and Remote Sensing*, GE-24(4), 462 – 472, doi:10.1109/TGRS.1986.289660, 1986.
- Randel, W. J., Seidel, D. J. and Pan, L. L.: Observational characteristics of double tropopauses, *J. Geophys. Res.*, 112(D7), D07309, doi:200710.1029/2006JD007904, 2007.
- Richards, M., Ackerman, S. A., Pavolonis, M. J. and Feltz, W. F.: Volcanic ash cloud heights using the MODIS CO2-slicing algorithm. [online] Available from: http://ams.confex.com/ams/Annual2006/techprogram/paper_104055.htm (Accessed 11 February 2011), 2006.
- Robock, A.: Volcanic eruptions and climate, *Reviews of Geophysics*, 38(2), 191–219, doi:10.1029/1998RG000054, 2000.
- Rose, W. I., Kostinski, A. B. and Kelley, L.: Real time C band radar observations of 1992 eruption clouds from Crater Peak/Spurr Volcano, Alaska, *U. S. Geological Survey Bulletin*, 2139, 19–26, 1995.
- Scambos, T. A., Dutkiewicz, M. J., Wilson, J. C. and Bindschadler, R. A.: Application of image cross-correlation to the measurement of glacier velocity using satellite image data, *Remote Sensing of Environment*, 42(3), 177–186, doi:10.1016/0034-4257(92)90101-O, 1992.
- Scharff, L., Ziemer, F., Hort, M., Gerst, A. and Johnson, J. B.: A detailed view into the eruption clouds of Santiaguito volcano, Guatemala, using Doppler radar, *J. Geophys. Res.*, 117(B4), B04201, doi:10.1029/2011JB008542, 2012.
- Scollo, S., Folch, A., Coltelli, M. and Realmuto, V. J.: Three-dimensional volcanic aerosol dispersal: A comparison between Multiangle Imaging Spectroradiometer (MISR) data and numerical simulations, *J. Geophys. Res.*, 115(D24), D24210, doi:201010.1029/2009JD013162, 2010.
- Scollo, S., Kahn, R. A., Nelson, D. L., Coltelli, M., Diner, D. J., Garay, M. J. and Realmuto, V. J.: MISR observations of Etna volcanic plumes, *J. Geophys. Res.*, 117(D6), D06210, doi:10.1029/2011JD016625, 2012.

Seiz, G., Tjemkes, S. and Watts, P.: Multiview Cloud-Top Height and Wind Retrieval with Photogrammetric Methods: Application to Meteosat-8 HRV Observations, *J. Appl. Meteor. Climatol.*, 46(8), 1182–1195, doi:10.1175/JAM2532.1, 2007.

Sparks, R. S. J.: *Volcanic plumes*, Wiley., 1997.

Stohl, A., Prata, A. J., Eckhardt, S., Clarisse, L., Durant, A., Henne, S., Kristiansen, N. I., Minikin, A., Schumann, U., Seibert, P., Stebel, K., et al.: Determination of time- and height-resolved volcanic ash emissions for quantitative ash dispersion modeling: the 2010 Eyjafjallajökull eruption, *Atmos. Chem. Phys. Discuss.*, 11(2), 5541–5588, doi:10.5194/acpd-11-5541-2011, 2011.

Teke, M. and Temizel, A.: Multi-spectral Satellite Image Registration Using Scale-Restricted SURF, in *Pattern Recognition (ICPR)*, 2010 20th International Conference on, pp. 2310 –2313., 2010.

Tupper, A., Carn, S., Davey, J., Kamada, Y., Potts, R., Prata, F. and Tokuno, M.: An evaluation of volcanic cloud detection techniques during recent significant eruptions in the western [']Ring of Fire', *Remote Sensing of Environment*, 91(1), 27–46, doi:10.1016/j.rse.2004.02.004, 2004.

Wu, B., Zhang, Y. and Zhu, Q.: Integrated point and edge matching on poor textural images constrained by self-adaptive triangulations, *ISPRS Journal of Photogrammetry and Remote Sensing*, 68(0), 40–55, doi:10.1016/j.isprsjprs.2011.12.005, 2012.

Wylie, D. P. and Menzel, W. P.: Two Years of Cloud Cover Statistics Using VAS, *Journal of Climate*, 2(4), 380–392, doi:10.1175/1520-0442(1989)002<0380:TYOCCS>2.0.CO;2, 1989.

Wylie, D. P., Santek, D. and Starr, D. O.: Cloud-Top Heights from GOES-8 and GOES-9 Stereoscopic Imagery, *J. Appl. Meteor.*, 37(4), 405–413, doi:10.1175/1520-0450(1998)037<0405:CTHFGA>2.0.CO;2, 1998.

Appendix A – conversion between geographic and geocentric Cartesian coordinates

Conversion from the geographic coordinates longitude λ , latitude φ , ellipsoid height h to the geocentric Cartesian coordinates X, Y, Z (Eq. A1):

$$\begin{aligned} X &= (N + h) \cdot \cos \varphi \cdot \cos \lambda \\ Y &= (N + h) \cdot \cos \varphi \cdot \sin \lambda \quad , \\ Z &= (N \cdot (1 - e^2) + h) \cdot \sin \varphi \end{aligned} \quad (A1)$$

where N is the radius of curvature in the prime vertical and e is the first eccentricity (Eq. A2)

$$\begin{aligned} N &= \frac{a}{\sqrt{1 - e^2 \cdot \sin^2 \varphi}} \\ e &= \sqrt{\frac{a^2 - b^2}{a^2}} \quad , \end{aligned} \quad (A2)$$

with a and b being the semi-major axis and the semi-minor axis of the reference ellipsoid.

Inverse conversion from the geocentric Cartesian coordinates to the geographic coordinates can be solved iteratively (Eq. A3):

$$h = \frac{\sqrt{X^2 + Y^2}}{\cos \varphi} - N$$

$$\tan \varphi = \frac{Z}{\sqrt{X^2 + Y^2} \cdot \left(1 - \frac{e^2 \cdot N}{N + h}\right)} \quad (\text{A3})$$

$$\tan \lambda = \frac{Y}{X}$$

Appendix B – list of MODIS datasets used to show the temporal evolution of the ACTH vertical distribution

Only MODIS datasets that cover a large portion of the ash plume were used for temporal evolution of ACTH vertical distribution (Fig. 8). Some datasets cover only a small area of the plume because of the swath's characteristics of Terra and Aqua satellite. Therefore, only selected MODIS datasets were used:

- MOD02QKM.A2010105.1135.005.2010105201236.hdf,
- MYD02QKM.A2010105.1330.005.2010106222502.hdf,
- MOD02QKM.A2010106.1220.005.2010106204119.hdf,
- MOD02QKM.A2010107.1125.005.2010108033632.hdf,
- MYD02QKM.A2010107.1315.005.2010109163206.hdf,
- MOD02QKM.A2010108.1205.005.2010108202240.hdf,
- MYD02QKM.A2010108.1400.005.2010109195617.hdf,
- MOD02QKM.A2010109.1250.005.2010110103338.hdf,
- MYD02QKM.A2010109.1305.005.2010111050209.hdf.

Figure captions

Figure 1. If an ash cloud is observed simultaneously from two satellites the position of the cloud seems to be shifted for a parallax when comparing both datasets. The parallax is a consequence of viewing geometries of both satellites and the height of the ash cloud.

Figure 2. Aggregation of MODIS data into SEVIRI's grid system; the ash cloud is marked by the red oval. Left above: an example of original MODIS data (part of MODIS band 1 data showing the Eyjafjallajökull ash cloud over the North Sea on April 15th 2010 at 11:35 UTC). Right above: A scheme of SEVIRI's point spread function – each dot represents a MODIS measurement, thus it is coloured according to its position within the SEVIRI pixel (dark purple dots represent greater weight than pale yellow dots). Left below: MODIS data transformed in the SEVIRI grid system (see the difference in the overall geometry that is a consequence of a difference in viewing angles of both instruments). Right below: SEVIRI data retrieved at approximately the same time as MODIS (11:27 UTC).

Figure 3: Schema of area-based image matching.

Figure 4. Refinement of shifts using image pyramids.

Figure 5. Volcanic ash dispersion on standard Flight Levels (3000 m – FL100, 6100 m – FL200, 10700 m – FL350, 16800 m – FL550) for the eruption of Eyjafjallajökull in April 2010. These ash dispersion data are a product of the VAAC London.

Figure 6. BTD (data for Apr. 15 at 20:00 UTC) reveals plumes dispersing at two different heights. Highly positive BTD values in dark blue over North Sea indicate ice crystals. Below it spreads a reddish plume with negative BTD.

Figure 7. SEVIRI data on Apr. 17th at 13:12 UTC (a); the cross-correlation index between the SEVIRI image and MODIS image retrieved at 13:15 UTC (b); optimal matching shift between both datasets in column direction (c); optimal matching shift between both datasets in line direction (d); parallax between both datasets (e); intersection distance between lines of sight projected to the north direction (f); ACTH for all available pixels (g); ACTH for pixels where intersection distance projected to the north direction is lower than 1.5 km. Please note that the fig. 7 b–d shows only *CI* and the shifts of the SEVIRI image retrieved before and not after the MODIS retrieval.

Figure 8. Another example of ACTH on Apr. 15th at 11:35 UTC (a) and on Apr. 19th at 12:50 UTC (b).

Figure 9. Vertical distribution of ACTH for the period between Apr. 15 and 19. All pixels are classified according to their ACTH in one of the 500 m height classes. Colours represent the relative amount of pixels within a class (in percent) – dark colours show that there are many pixels in a height class. Because of two daytime MODIS overpasses two ACTH estimations can be done per day. On Apr. 16th only one estimate is presented because of the unfavourable satellite's swath characteristics. The highest measured heights by the radar (Marzano et al., 2011) are shown for the comparison.
(a)

Figure 10. ACTH error coefficient as a function of the latitude.

Figure 11. ACTH difference between the case study estimate and MISR measurements on Apr. 19th at 12:50 UTC.

Figure 12. Comparison of the valid ACTH of the ash plume and the standard MODIS top height product (a) and results of the BT method (b) on Apr. 15th at 11:35 UTC (ACTH in fig. 8a).